The rate and extent of windgap migration regulated by tributary confluences and avulsions

Eitan Shelef[1] and Liran Goren[2]

[1]Department of Geology and Environmental Science, University of Pittsburgh, Pittsburgh, PA, 15217
[2]Department of Earth and Environmental Sciences, Ben-Gurion University of the Negev, Israel, 84105

Correspondence: Eitan Shelef (shelef@pitt.edu)

Abstract. The location of drainage divides sets the distribution of discharge, erosion, and sediment flux between neighboring basins, and may shift through time in response to changing tectonic and climatic conditions. Major divides commonly coincide with ridgelines, where the drainage area is small and increases gradually downstream. In such settings, divide migration is attributed to slope imbalance across the divide that induces erosion rate gradients. However, in some tectonically affected region, low-relief divides, windgaps, abound in elongated valleys, whose drainage area distribution is set by the topology of large, potentially avulsing side-tributaries. In this geometry, distinct dynamics and rate of along-valley windgap migration is expected, but this process remains largely unexplored. Inspired by field observations, we investigate along-valley windgap migration by simulating the evolution of synthetic and natural landscapes, and show that confluences with large side tributaries influence migration rate and extent. Such confluences facilitate stable windgap locations that deviate from intuitive expectations based on symmetry considerations. Avulsions of side tributaries can perturb stable windgap positions and avulsion frequency governs the velocity of windgap migration. Overall, our results suggest that tributaries and their avulsions may play a critical role in setting the rate and extent of windgap migration along valleys and thus the time scale of landscape adjustment to tectonic or and climatic changes across some of the most tectonically tectonically most affected regions of Earth, where windgaps are common.

1 Introduction

Drainage divides play a pivotal role in controlling the geometry of fluvial landscapes and shaping their hydrologic and geomorphic functionality. Divides' location, and as a consequence, basins' geometry, are transient features of the landscape (e.g., *Willett et al.*, 2014; *Whipple et al.*, 2017) that respond to shifting boundary conditions. As early as the late 19th century, *Gilbert* (1877) and *Davis* (1889) described divide migration and drainage reorganization, and since then, the geomorphology literature has documented many examples of such drainage network reorganization at both the local-scale (e.g., *Johnson*, 1907; *Woodruff*, 1977; *Nugent*, 1990; *Brocard et al.*, 2011; *Prince et al.*, 2011; *Yanites et al.*, 2013; *Schmidt et al.*, 2015; *Forte et al.*, 2015; *Fan et al.*, 2018) and the regional-scale (e.g., *Ollier*, 1995; *Zelilidis*, 2000; *Shephard et al.*, 2010; *Clark et al.*, 2004; *Liu*, 2014; *Yang et al.*, 2020).

Whereas drainage divides could be breached abruptly via river capture events (e.g., *Bishop*, 1995; *Prince et al.*, 2010; *Willett*

25 *et al.*, 2014), a possibly more common process involves long-lasting and continuous divide migration at basins headwaters, where the divides are located along ~~ridge lines~~ ridgelines (e.g., *Willett et al.*, 2014; *Goren et al.*, 2014b; *Shelef and Hilley*, 2014; *Whipple et al.*, 2017; *Beeson et al.*, 2017; *Braun*, 2018). In these high relief settings, divide migration is linked to an imbalance in erosion rate across the hillslopes that bound the divide (*Forte and Whipple*, 2018). Hillslope erosion and slope are linked to incision at the proximal channel head (the local base level for the hillslope). Given that channel erosion rate

30 scales with channel gradient and drainage area (a proxy for discharge, (e.g., *Howard*, 1994; *Whipple and Tucker*, 1999)), small across-divide differences in these factors can lead to disparate channel incision rates across the divide and to a gradual divide migration directed from the ~~fast to the slow~~ rapidly eroding to the slowly eroding hillslope (*Beeson et al.*, 2017; *Braun*, 2018).

Over long timescales, feedbacks might arise that promote a prolonged and gradually declining divide migration (*Willett et al.*, 2014; *Whipple et al.*, 2017). An area-feedback occurs as the basin at the side of the ~~fast~~ rapidly eroding hillslope grows (here-

35 after the ~~aggressor~~ expanding basin), whereas its across-divide neighbor shrinks (hereafter the ~~victim~~ shrinking basin) (*Willett et al.*, 2014; *Yang et al.*, 2015; *Whipple et al.*, 2017). An increase in the ~~aggressor's~~ expanding basin drainage area, increases its erosion rate and promotes further divide migration and area gain ~~(Mudd and Furbish, 2005; Whipple et al., 2017; Goren et al., 2014b)~~ ~~. The opposite process operates at the victim basin that losses drainage area~~ (*Willett et al.*, 2014; *Mudd and Furbish*, 2005; *Whipple et al.*, 20 . The complementary process operates on the shrinking basin that loses drainage area and becomes susceptible to further area

40 loss by continuous divide migration and side captures. Parallel to this area-feedback, which furthers divide migration, a channel length-feedback arises which gradually suppresses this migration. As the divide migrates, ~~the victim basin shortens and the aggressor~~ channels of the shrinking basin shorten and channels of the expanding basin lengthen, which increases the overall gradient of the ~~victim~~ shrinking basin compared to the ~~aggressor~~ expanding basin, eventually leading to a balance in erosion rate across the divide so the divide migration stops. The relative magnitude of these competing area and length feedbacks

45 changes gradually through the migration process, and thus the velocity of divide migration typically declines smoothly through time (*Braun*, 2018). This gradual divide migration process is associated with settings ~~whereby~~ in which the migrating divide is located along a ridgeline that is topographically higher than the tributaries draining to the ~~victim~~ shrinking basin. Migration then erases the morphology and topology of the ~~victim~~ shrinking basin and obliterates the antecedent course of ~~victim basin's~~ its tributaries (Figure 1~~a~~a-b).

50 A distinctly different dynamic is expected to emerge when a drainage divide forms a deep saddle within a valley (a windgap, (e.g., *Bishop*, 1995)). In such settings, the windgap is lower than the ridges that bound the valley ~~,~~ and thus the morphology of the bounding ~~ridge lines~~ ridgelines and the tributaries that drain them into the valley can be ~~preserved despite windgap migration~~ largely preserved as the windgap migrates along the valley (e.g., *Harel et al.*, 2019) (Figure 1~~b~~c-d). The preserved side tributaries can cause punctuated changes in drainage area through the divide migration process that distinctively differ from

55 the aforementioned gradual exchange of drainage area. We thus intuit that the coupled dynamics of side tributaries draining close to a windgap and windgap migration could be key in controlling windgap stability, migration velocity and the evolution of valley topography.
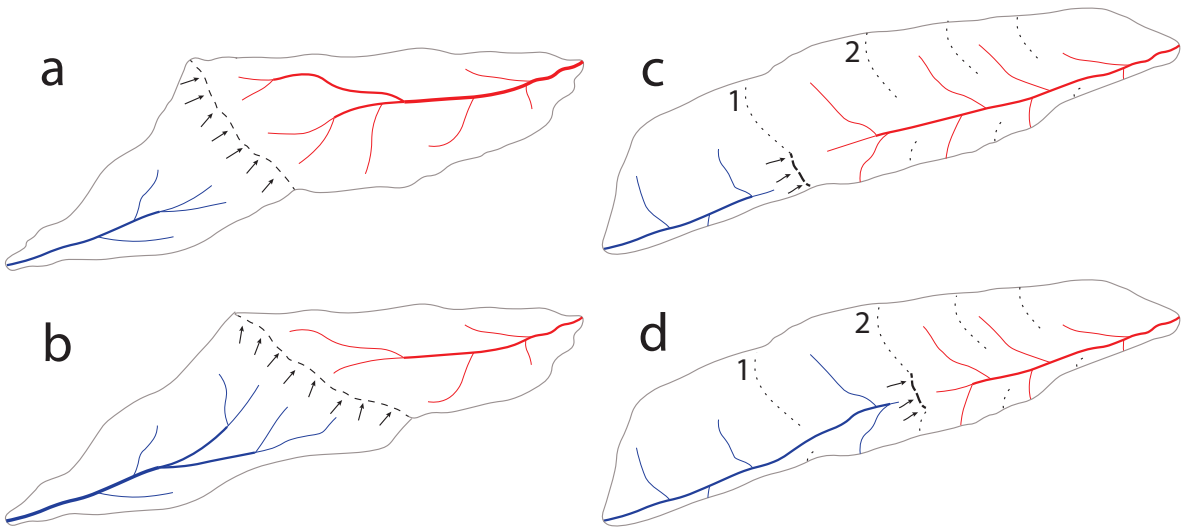
Figure 1. Schematic illustration of a typical (a,b) vs. along valley (c,d) divide migration. (a) Illustration of a typical divide migration process where the divide (dashed line) is located along a ~~ridge line~~ ridgeline (after *Whipple et al.* (2017)). (b) The same setting as in panel a, after the divide migrated some distance. Note that as the ~~ridge line~~ ridgeline migrates it erases the tributaries of the ~~victim~~ shrinking basin. (c) Illustration of a windgap (dashed line) migration along a valley. Note that the tributaries that drain to the valley can be preserved through the migration process, so that the migrating windgap can traverse confluences with tributaries through its migration. (d) Same setting as in panel c, after the windgap migrated some distance. Low order channels are marked with thinner lines. Note that the low order drainage divides between tributaries (dotted lines) can merge with the migrating windgap to form a high order divide (for example, see the low order divides marked 1 and 2 in panels c and d)..

Windgap migration along a valley is likely common in tectonically active and/or structurally deformed areas where windgaps are prevalent. Such migration is likely facilitated by relatively erodible bedrock or sediments within valleys (*Harel et al.*, 2019), or may be induced by tilting in tectonically active areas (*Bishop*, 1995; *Clark et al.*, 2004). Windgaps are found along longitudinal, structurally controlled valleys as well as in antecedent highland valleys truncated by cliffs or formed by large capture events (e.g., *Haworth and Ollier*, 1992; *Bishop*, 1995; *Prince et al.*, 2010; *Harel et al.*, 2019) (e.g., Figure 2). The location and migration of windgaps dictate the distribution of erosion, discharge, and sediment fluxes between diverging regional to continental scale drainage networks and sedimentary basins, and may therefore set a primary control on the geologic evolution of some of the most active regions on Earth. Yet, the dynamics of windgap migration remain largely unexplored.

In this study we ~~set~~ seek to identify and explore key aspects of the dynamics of windgap migration. In particular, we focus on the influence of confluences and avulsions of side tributaries on the rate and extent of windgap migration.
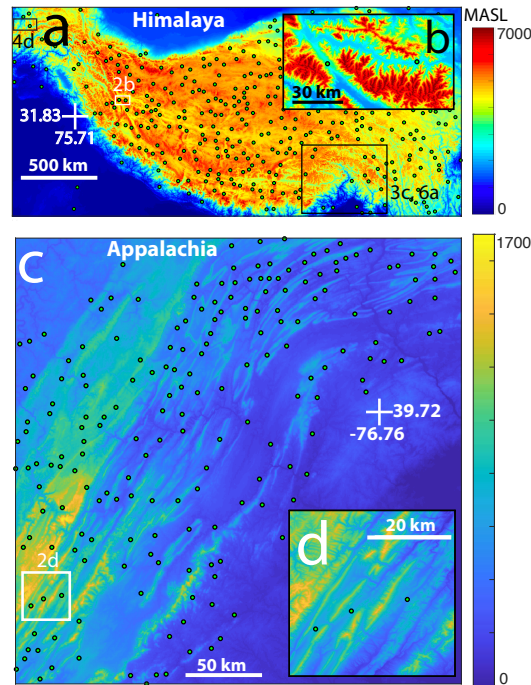
Figure 2. Windgaps in tectonically influenced areas. (a) A map of estimated windgap locations (yellow circles) in the Himalaya. ~~The inset box at~~ Boxes mark the ~~bottom right marks the areas~~ regions shown in ~~other~~ figures 3c and ~~6, and the~~ figure numbers are specified next to each box~~at~~. (b) a zoom into the ~~upper left marks~~ section of the ~~area shown~~ map marked 2b in ~~Figure 4d-e~~panel a , showing a more detailed view (using an SRTM DEM (*Farr et al.*, 2007)) of windgap locations. Here, the colorbar represent the range of elevations between 3500m and 6000m. (~~b~~c) A map of estimated windgap locations in the Appalachian ~~fold-thrust~~ fold and thrust belt. ~~Windgaps locations were identified over GMTED DEMs (*Danielson and Gesch*, 2011) by delineating~~ (d) A zoom into the ~~drainage divides associated with a channel network mapped with drainage area thresholds~~ section of ~~200 and 12.5 km² for the Himalayas and Appalachia~~map marked 2d in panel c, ~~respectively showing a more detailed view (~~values hereafter are reported in the same order for these two areas~~using an SRTM DEM (*Farr et al.*, 2007)) of windgap locations. ~~To identify major divides at relatively low topographic positions (i.e.~~Here, ~~windgaps) we isolated high order divides (*Scherler and Schwanghart*, 2020), computed~~ the ~~local relief based on divide elevations within a radius~~colorbar represent the range of ~~30~~ elevations between 450m and ~~5 km, respectively, and identified locations of minimal divide elevation within these radii~~1500m. ~~These radii are based on typical valley widths in these areas and are similar~~ Color schemes were selected to highlight the ~~typical distance from divide to channel head based on the drainage area threshold that was used to define channels (scaled to distance via Hack's law)~~specific topography of every regions. ~~Of the~~ Windgaps locations ~~of minimal divide elevation, we~~ were identified ~~windgaps as locations with low along valley relief~~ over GMTED DEMs (*Danielson and Gesch*, 2011) ~~and high across valley relief, to do so, we identified locations~~ are only a subset of ~~local divide relief that is higher than 200 and 100 m, respectively (i~~all windgaps in these regions. ~~e., common low-end reliefs~~ The procedure used for ~~noticeable valleys~~ automated windgap identification is described in ~~these areas), and a vertical elevation difference between~~ the ~~divide and closest streams~~ supplementary information file (~~on each side of the divide~~SI)~~that is less than 20% of the local divide relief~~.

2   Field observations

This study is inspired by field observations of windgaps that traversed confluences with side tributaries along their migration
70   pathway. Along the Arava escarpment, Israel, antecedent valley systems were beheaded ~~during a regional~~as part of a regional, long-lasting, drainage reorganization associated with the escarpment's development (*Ginat et al.*, 2000; *Avni et al.*, 2000; *Harel et al.*, 2019)~~, forming numerous windgaps that~~. Numerous windgaps are aligned with the escarpment cliff~~. Some of the windgaps~~, some of which migrated inland along antecedent valleys (*Harel et al.*, 2019), traversing confluences with side tributaries. Observations from Wadi Grofit, for example, show that several confluences were traversed by a migrating windgap,
75   as seen by their barbed morphology (Figure 3a-b). A similar setting, albeit at a much larger scale, is observed at the eastern syntaxis of the ~~Tibetan Plateau~~Himalaya. Here, the Parlung-Siang-Lohit river capture (*Lang and Huntington*, 2014; *Schmidt et al.*, 2015; *Govin et al.*, 2018; *Zhang et al.*, 2019) (Figure 3c) triggered a windgap migration of more than 200 km along the Parlung valley. Through its migration, the windgap traversed confluences with side tributaries that may have influenced the migration dynamics.

80   This study is further motivated by field observations showing that avulsions of side tributaries can shift discharge across windgaps. Such a setting is observed, for example, along an east-west directed valley, next to Mt. Berech on the highlands of the Arava escarpment. Here, avulsions occur at the head of an alluvial fan that is formed at the mouth of a side tributary~~that drains~~, draining into a valley close to a windgap. ~~The~~ While most of the tributary discharge is still routed to the valley side that drains away from the escarpment, the avulsions route a fraction of the discharge ~~of the side tributary~~across the windgap
85   to the escarpment side ~~of a windgap~~ (Figure 4a-c)~~, where the magnitude of incision appears to be comparably high~~. A similar example, of a somewhat larger scale, is observed in the Hindu-Kush province of the Himalaya, next to the Ishkashim Pass windgap, Afghanistan. Here, a side tributary forms an alluvial fan as it drains into an east-west directed valley, and avulsions at the apex of this fan route discharge across a windgap (Figure 4d-e). We intuit that such avulsions can modify the relative erosion rates across windgaps and thus the rate and extent of windgap migration.

90   The observations described above (Figures 3 and 4), and the realization that windgap migration may be a ~~prominant~~ prominent mechanism of landscape development in tectonically active and structurally deformed regions (Figure 2), inspired simulations that explored how the dynamics of windgap migration are influenced by: (a) confluences with side tributaries, and (b) avulsions of such side tributaries across windgaps.
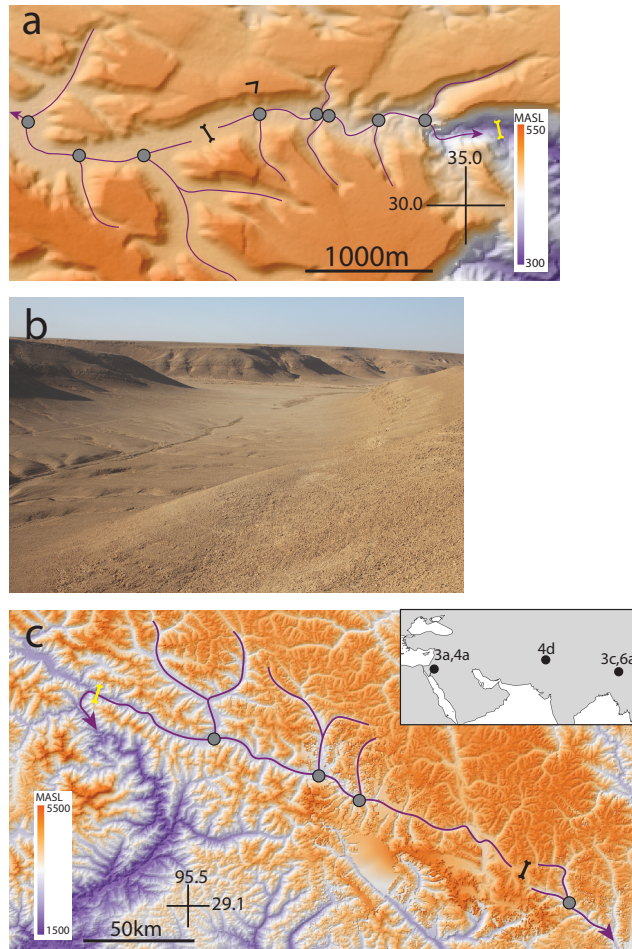
Figure 3. Examples of valleys with windgaps and major confluences with side tributaries (grey circles). Major channels are marked in ~~blue~~ purple and their flow direction is marked with an arrow. (a) A map, based on a TanDEM-X DEM (*Krieger et al.*, 2007), showing an example from wadi Grofit in the Negev highlands along the Arava escarpment, Israel. The current location of the windgap is marked by a bold forked black line. The approximated initial location of the windgap is marked with a ~~thin~~ forked ~~black~~ yellow line (*Harel et al.*, 2019). A black v-shaped symbol open to the south-west shows the locations from which the pictures in panels b was taken. (b) A picture of the windgap shown in panel a~~, taken~~. Note the low relief of the windgap and a side tributary that joins the valley from the ~~location~~ left hand side of the ~~aforementioned black v-shaped symbol towards south-west~~picture. (c) A map, based on GMTED2010 DEM (*Danielson and Gesch*, 2011), showing ~~windgaps~~ the windgap and confluences along the Parlung valley, China. ~~The current location of the windgap is marked by~~ Windgap symbols are as in panel a~~bold forked black line. A thin forked black line at the north-west portion of the map marks the approximate initial location of the windgap.~~ In both the Grofit and Parlung ~~exampels~~examples, the windgap likely traversed confluences with side tributaries (grey circles), resulting in their barbed morphology~~, as it migrated to its current location~~. The inset map shows the general location of the field examples presented in this and other figures, figure numbers are specified next to each location.
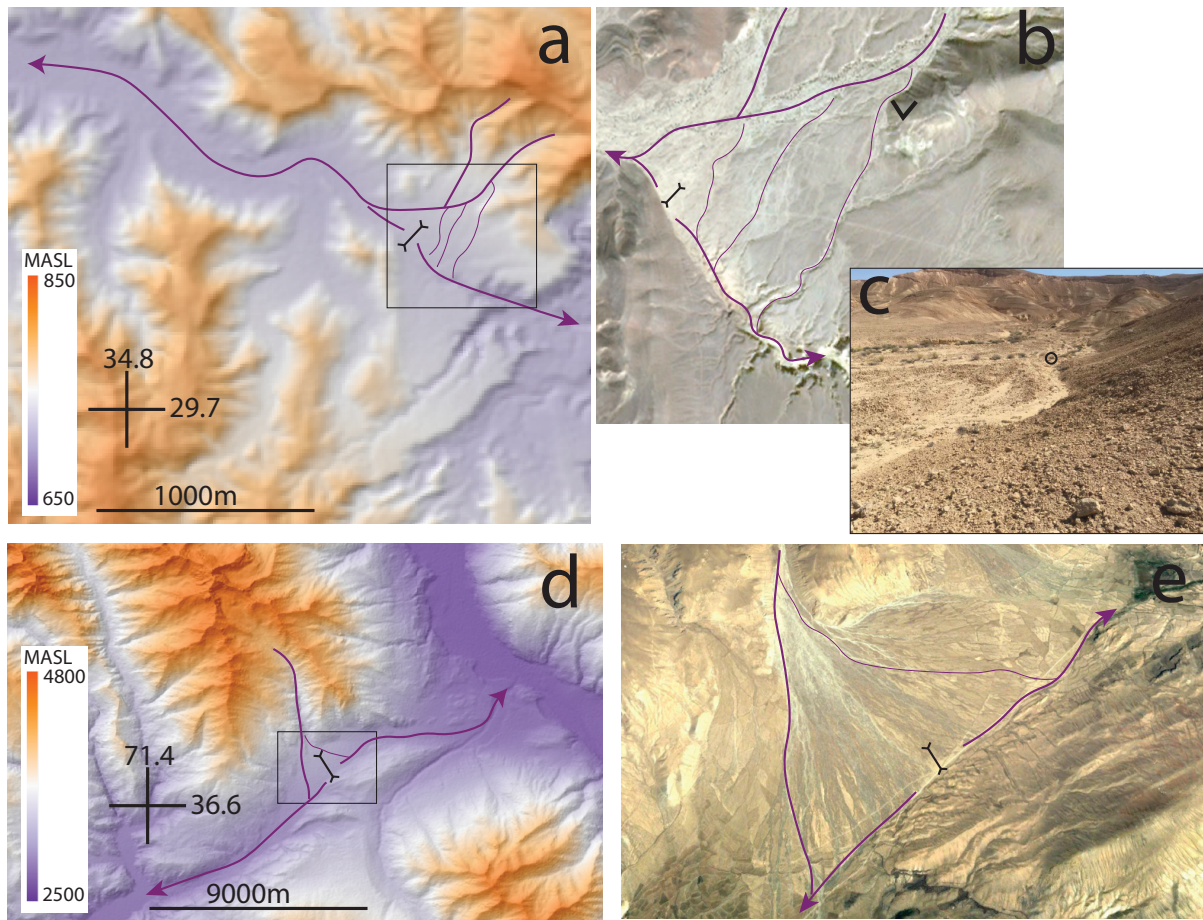
Figure 4. Examples of avulsions across windgaps (forked black line). Channels are marked in ~~blue~~purple. (a) A map, based on a TanDEM-X DEM *(Krieger et al., 2007)*, of a windgap next to Mt. Berech in the Negev hilghlands along the Arava escarpment, Israel. Note that although the side tributaries ~~marked in blue~~ drain primarily north-west of the windgap, few bifurcating branches appear to route a fraction of the tributaries' discharge to the other side of the windgap. Black box marks the area shown in panel b. (b) An airphoto (©Google Earth 2020) showing the main channels of the side tributaries as well as their bifurcating branches. A black v-shaped symbol open to the north shows the locations from which the picture in panels c was taken. (c) View of an avulsion point looking upstream (north) from the aforementioned v-shaped symbol. Circle marks a backpack for scale, that is located at the bifurcation point. (d) A map, based on a GMTED2010 DEM *(Danielson and Gesch, 2011)*, of the Ishkashim Pass area in Afghanistan. Note that although the side tributary ~~(marked in blue)~~ drains primarily south-west of the windgap, few bifurcating branches appear to route a fraction of its discharge to the other side of the windgap. Black box marks the area shown in panel e. (e) An airphoto (©Google Earth 2020) showing the bifurcation of a side tributary across the windgap.

3 Method

To investigate the influence of side tributaries on the velocity and extent of windgap migration, we use a landscape evolution model (e.g., *Tucker and Hancock*, 2010; *Perron et al.*, 2009):

$$\frac{dz}{dt} = U - (KA^m S^n - D\nabla^2 z). \tag{1}$$

In equation (1), $\frac{dz}{dt}$, the change in elevation, z [L], through time, t [T], is a function of uplift rate, U [L/T], channel incision through detachment limited processes, $KA^m S^n$ [L/T], and changes in elevation due to diffusive sediment transport, $D\nabla^2 z$ [L/T] that likely dominates hillslope settings. In this model, channel incision is a function of drainage area, A [L^2], and topographic gradient, S, as well as an erodibility coefficient, K [L^{1-2m} T^{-1}]. The two exponents, m and n acknowledge that erosion may be a non-linear function of drainage area and gradient, respectively (*Howard and Kerby*, 1983; *Seidl and Dietrich*, 1992; *Howard*, 1994). Sediment transport is modelled as a diffusive process, where D [L^2 T^{-1}] is a diffusion coefficient, and $\nabla^2 z$ [L^{-1}] is the laplacian of elevation (*Culling*, 1963; *Howard*, 1994). We use a finite difference scheme, where drainage area is the summation of the area of all upstream nodes, and topographic gradient is computed via a forward difference scheme in the downslope direction. The drainage area of the divide node is bifurcated between neighboring nodes according to the relative magnitude of the slope to each neighboring node ~~raised to a power of 1.1~~ (i.e., *Freeman*, 1991). This is a conservative choice that aims to minimize the influence of spatial discretization on windgap stability (i.e., *Pelletier*, 2004). The model integrates equation (1) through time using a 4-5 order explicit Runge-Kutta integration where time-stepping is constrained by the Courant criteria. The parameters K, m and n are determined based on common values published in the literature, D is scaled based on the values of K and m so that comparable models have the same length (L_p) associated with a Péclet value of unity (i.e., $L_p = \left(\frac{D}{K}\right)^{\frac{1}{2m+1}}$ after *Perron et al.* (2008, 2009)). We set this length to be relatively short (200-500 meters) such that diffusive sediment transport is generally negligible within channels. The values of the parameters used in different simulations are reported in ~~the captions of the figures that present these simulations.~~ Table 1.

To explore how confluences with side tributaries ~~influences~~ influence the migration velocity and stable positions of windgaps, we first simulate the evolution of a synthetic 1-dimensional landscape with such confluences (hereafter 'fixed confluence simulations'). The initial setting (Figure 5a,b) is of an elongate valley, where the windgap is at the left edge of the valley, bounded by a cliff to its left, and a trunk channel drains the valley to the right (Figure 5b, case 1). The initial topography of the trunk channel is set to be at a topographic steady state (i.e., $dz/dt = 0$) in accordance with equation (1). The boundary conditions are set to a constant and equal elevation at both ends of the model. The topology of the valley-tributary system is prescribed as a set of equally spaced trunk-tributary confluences along the valley, where tributaries have the same drainage area (i.e., the drainage area added at the confluence) (Figure 5a)~~and the~~. The valley has a constant width and thus non-confluence nodes are all assigned the same local drainage area. The deviation of this topology from a Hack scaling (i.e., *Hack*, 1957) is supported by field observations (i.e., Figures 3, 4) and ~~also~~ contributes to the simplicity of this synthetic model setting.

We varied the tributaries drainage area between simulations and recorded the velocity of windgap migration and the location where the windgap attains a stable position. A stable position is defined as where the windgap position is fixed and the elevation difference between consecutive time steps is everywhere zero for 100 consecutive time steps. ~~We explored the influence of the~~

Figure	U [m yr^{-1}]	D [m^2 yr^{-1}]	K [m^{1-2m} yr^{-1}]	m []	n []	L_c [m]	L [m]	W [m]	A_t [m^2]	Δx [m]	Δt_a [yr]
5	1×10^{-3}	2.4×10^{-1}	1×10^{-5}	4.5×10^{-1}	1	2.875×10^4	6.4×10^3	4×10^2	5.12×10^6	1×10^2	50*
6c	5×10^{-3}	2	7.96×10^{-6}	5×10^{-1}	1	6.225×10^5	-	-	-	5×10^2	50*
7a-b	1×10^{-3}	2.4×10^{-1}	1×10^{-5}	4.5×10^{-1}	1	2.875×10^4	6.4×10^3	4×10^2	**	1×10^2	-
7a-b	1×10^{-3}	6.8×10^{-1}	1×10^{-5}	5.5×10^{-1}	1	2.875×10^4	6.4×10^3	4×10^2	**	1×10^2	-
7c	1×10^{-3}	2.4×10^{-1}	1×10^{-5}	4.5×10^{-1}	1	2.875×10^4	6.4×10^3	4×10^2	5.12×10^6	1×10^2	***
8	1×10^{-3}	2.4×10^{-1}	1×10^{-5}	4.5×10^{-1}	1	2.875×10^4	6.4×10^3	4×10^2	5.12×10^6	1×10^2	50*

Table 1. Table of model parameters. U: uplift rate; D: diffusion coefficient; K: erodibility coefficient; m, n, drainage area and slope exponents, respectively; L_c: distance to the center of model domain; L: distance between confluences; W: valley width; A_t: tributary area; Δx: node spacing; Δt_a: time between avulsions; *: only for models with avulsions; **: varying drainage area where the lowest value is the same as the drainage area of a single non-confluence node (i.e., $W \times \Delta x$) and all following values range from 2 to 20 segment areas (i.e., $L \times W$), in steps of $2 \times L \times W$; ***: varying time between avulsions (between 50 to 950 years in intervals of 100 years).

~~scaling between erosion rate and drainage area by varying the value of the area exponent m (0.45, 0.55).~~ Simulation results are compared to a reference simulation, where there are no confluences with side tributaries, the ~~local drainage area is identical for all model nodes, and the~~ total drainage area is equal to the equivalent simulation with trunk-tributary confluences and is distributed equally between all model nodes.

To study the influence of avulsions of side tributaries on the rate and extent of windgap migration, we simulated such avulsions by shifting the location of trunk tributary confluences through time (hereafter, 'avulsion simulations'). To achieve ~~this~~ these dynamics, we randomly varied the confluence location within a prescribed distance from its initial position. The random distances are selected from a uniform distribution centered at the original location of each confluence, and the maximal distance is constrained to half the distance between the original location of confluences (i.e., Figure 5a). Avulsions occur in all tributaries, regardless of their location relative to the windgap. We explored the influence of the time span, Δt_a, between avulsions (i.e., shifts in confluence location) by varying it between simulations (from 50 to ~~500~~ 950 yrs). We explored the influence of model parameters in all three versions of the simulations (reference, fixed confluence, and avulsions) with two different m values (m=0.45, m=0.55) for eleven different values of tributary area/segment area ratio in the fixed confluence simulations and ten values of time span between avulsions in the avulsion simulations (Table 1). Simulation results of varying the slope exponent, n, are presented in the Supplementary Information.

An independent set of simulations is dedicated to exploring the potential influence of tributary confluences on windgap migration in a natural setting. Here, the topology of the aforementioned Parlung-Siang-Lohit system is used as a template for the simulation, and we focus on the system dynamics following the Parlung-Siang-Lohit capture (*Lang and Huntington*, 2014; *Schmidt et al.*, 2015; *Govin et al.*, 2018; *Zhang et al.*, 2019) (Figure 6a-b). The initial conditions (Figure 6d) replicate the inferred channel-system topography and topology at the time of the capture. For this 'natural' experiment, we assume that (a) the ~~aggressor~~ expanding (Siang river) and ~~victim~~ shrinking (Parlung river) basins ~~where~~ were approximately at a topographic steady state at the time of capture, (b) the capture occurred at point d in Figure 6a, (c) the channels' profile could

150   be reconstructed based on equation (1), and (d) the location and drainage area of tributary confluences were similar to the present-day tributary confluence configuration. The confluence between the Siang and Lohit-Parlung (point f in Figure 6a) is used as the boundary conditions for these simulations. We extract the drainage area along the rivers from a GMTED2010 DEM (*Danielson and Gesch*, 2011) with a resolution of 15 arc-seconds (approximately 500 m). We slightly modified the DEM to correct inaccuracies in basin boundaries close to the headwater of the Parlung river. The choice of model parameters (see

155   ~~caption of Figure 6~~Table 1) is coarsely guided by values suggested in the literature (*Wang et al.*, 2017; *Govin et al.*, 2018; *Yang et al.*, 2018; *Zhang et al.*, 2019) and adjusted to the present-day relief. Note that this simulation aims to demonstrate the potential influence of network topology on windgap migration in a natural setting, and not to investigate the development of the Parlung-Siang-Lohit capture specifically.
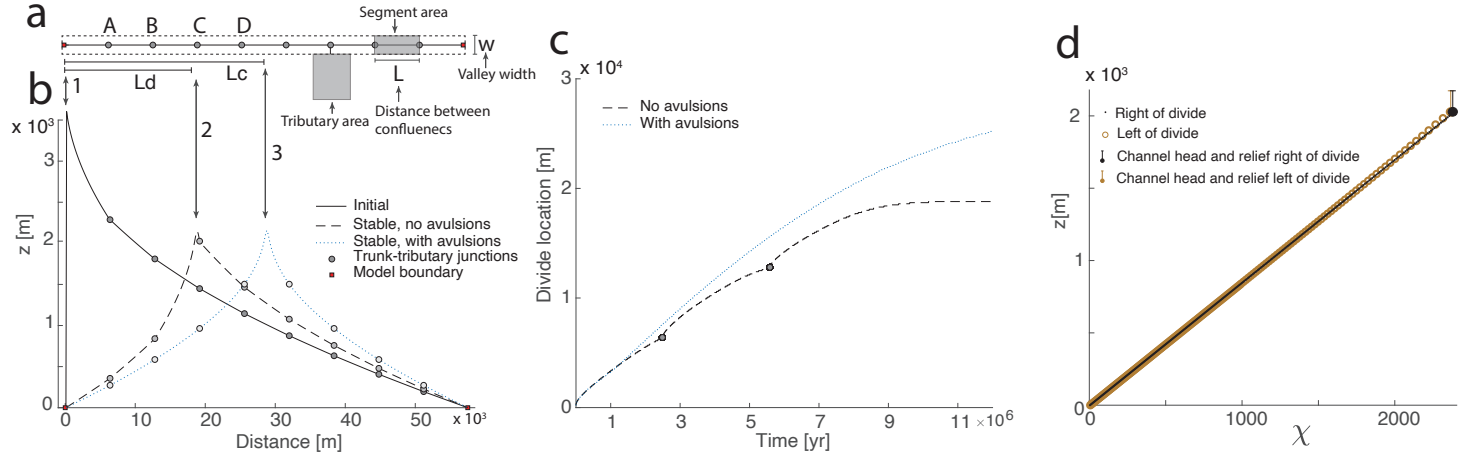
Figure 5. Simulations of along valley windgap migration across confluences with tributaries. (a) Plan view schematic of a 1-dimensional model domain that simulates a valley ~~(valley boundaries marked by a dashed line)~~ of constant width (w) that is drained by a trunk channel (dark line) with equally spaced (L) confluences with tributaries~~(grey circles)~~. The drainage area of ~~a segment~~ nodes between confluences is fixed ~~($L \times w$~~ $\Delta x \times w$, ~~schematically represented by a grey rectangle~~see Table 1 for values of model parameters~~)~~. The drainage area of a tributary is the local area that is added at each confluence (an example is represented here by a grey rectangle). L_d and L_c mark the distance from the left edge of the model domain to the location of a stable windgap position and to the center of the model domain, respectively~~, and are referred to in figures 7 and 8~~. Confluences marked A-D are referred to in figure 7a. (b) An example of simulated topographic profiles along the trunk channel: (1) A topographic profile of the simulation's initial condition~~(solid line, trunk-tributary confluences marked by dark grey circles)~~; (2) Simulated steady state topography that develops from the initial condition in profile #1 through a fixed ~~confluences~~ confluence simulation~~(dashed line, trunk-tributary confluences marked by medium grey circles)~~. Note that the windgap attains a stable position away from the center of the model domain (i.e., $L_d < L_c$). Also note that this steady position occurs adjacent to a trunk-tributary confluence on the ~~victim's~~ shrinking side of the windgap; (3) Simulated steady state topography with avulsions (~~dotted line,~~ light gray circles mark the mean location of trunk-tributary confluences - which is the same as that of the fixed ~~confluences~~confluence). The windgap's stable position is at L_c. (c) Simulated windgap location vs. time for the simulations in panel b. ~~For the fixed confluences simulation (solid line), note the changes in windgap migration velocity (i.e., the gradient of the line in the figure) as the windgap migrates across tributary confluences (grey circles).~~ Note that ~~these changes in migration velocity are not apparent in a simulation with avulsions (dashed line) and that~~ the ~~overall windgap velocity is higher when avulsions are simulated. Note that the~~ plot shows the model duration until the windgap in the fixed ~~confluences~~ confluence simulation attained a stable position (case 2 in panel b)~~, and that in the avulsions simulation the windgap continued migrating until it attained a stable position at the center of the model domain (case 3 in panel b, at a distance of about 30 km from the initial windgap location)~~. (d) A $\chi - z$ plot (*Perron and Royden*, 2013) for case 2 in panel b. ~~The plot demonstrates that this windgap position is stable although it is not in the center of the model domain.~~ Note that the relief from each channel head to the windgap is also marked (see legend). The channel head is defined based on where the topographic profile shifts from concave to convex. The channel head right of the divide (a black filled circle in the $\chi - z$ plot) is at the adjacent tributary confluence~~(grey filled circle just right of the divide in profile 2, panel b)~~. ~~Panels a-d~~Model parameters are ~~based on a model configuration with 8 trunk-tributary confluences (4 at each side of the model center), 575 model nodes, node spacing: $\delta x = 100$, confluence spacing: $L = 6400$ m, valley width: $w = 400$ m, tributary area equals 2 segment areas (i.e., $2 * L \times w$), hillslope diffusion coefficient: $D = 0.24$ m^2 yr^{-1}, exponents: $n = 1$, $m = 0.45$, channel erodibility: $K = 1 \times 10^{-5}$ m$^{0.1}$ yr^{-1}, time interval between avulsions 50 yr.~~ given in Table 1.

HSimulated windgap migration along the Parlung valley. (a) A regional map, based on 15 arc-second GMTED2010 DEM (approximately 500 m resolution) showing the Yigong, Parlung, Lohit, Siang and Yarlung rivers (location is shown as a box in figure 2a). Reconstructions of a paleo-drainage pattern (*Lang and Huntington*, 2014; *Govin et al.*, 2018; *Zhang et al.*, 2019) suggest that the Yigong and Parlung used to drain southeast to the Lohit, until the Yigong was captured by the Siang river. This created a windgap at the top of the beheaded Parlung valley, just east of the capture point. The approximate capture location is marked by point d. Point e marks the current location of the windgap between the north-west flowing Parlung and south-east flowing Lohit rivers. Point f marks the confluence of the Lohit and Siang rivers. Thin dark lines mark river systems with drainage area larger than 10^8 m^2, and the bold dark lines mark the river system that is simulated in panel c. A black rectangle marks the area shown in panel b. (b) Map of the Parlung river basin. The Parlung reversed its flow direction following the capture, likely through windgap migration from the capture point (point d) to the current location of the windgap (point e). As the windgap migrated, portions of the valley that used to drain eastward through the Lohit reversed their flow direction. Points 1, 2 and 3 mark simulated stable windgap locations in conjunction with panel c. The labels t1, and t2, mark large tributaries of the Parlung river. (c) Profiles of simulated initial and steady-state topography. The symbol f marks the model boundaries at the location of the Lohit-Siang confluence, as shown in panel a. The symbols d, 1, 2, 3, mark the windgap locations, in conjunction with panel b, for the cases of: d – a profile at the time of capture of the Yigong-Parlung by the Siang (the initial topography of the simulations); 1 – a profile of a simulated stable windgap position that develops after the Yigong-Parlung capture caused eastward windgap migration along the Parlung valley. Note that this stable location is just west of a confluence with a large tributary (t1). The confluence location is shown in panel b (point 1) and marked with a yellow circle on the topographic profile in panel c); 2 – a stable windgap position that developed by simulating an avulsion (i.e., shifting the confluence of tributary t1 to the aggressor's side of the windgap: left of the windgap location in profile 1). Note that this new stable windgap position is just west of a confluence with a large tributary t2 (the confluence location is shown in panel b and marked with a yellow circle on the topographic profile in panel c). 3 – a stable windgap position that is attained through avulsion simulation, where tributaries with drainage area larger than 10^7 m^2 are allowed to avulse. The simulations use the following parameters: $n = 1$, $m = 0.5$ (e.g., *Wang et al.*, 2017; *Yang et al.*, 2018), $\delta x = 500$ m (i.e in accordance with DEM resolution), $D = 2$ m^2 yr^{-1}, $K = 7.96 \times 10^{-6}$ yr^{-1}, $U = 0.005$ m yr^{-1}.

4 Results

Fixed confluence simulations with synthetic topography show that trunk-tributary confluences affect the velocity of windgap migration. Analysis of the windgap location through time (Figure 5c) shows that the velocity of windgap migration decreases as it approaches a trunk-tributary confluence at the ~~victim's~~ shrinking side, and increases as the windgap migrates across a confluence. At a larger scale, the migration velocity decreases as the windgap migrates further from its initial location and closer to the center of the model domain (Figure 5a-d). Importantly, we observe that in cases where the windgaps do not reach the center of the model domain, it attains a stable position close to a confluence with a tributary that drains to the side of the ~~victim~~ shrinking basin.

The same simulations further show that the tributaries drainage area influence the location where the windgap attains a stable position, as well as the mean windgap migration velocity (Figure 7a,b). Figure 7a shows that as the relative drainage area of tributaries increases, the stable windgap position is farther away from the center of the model domain (i.e., closer to the left

195 side of the model, Figure 5). The figure also shows that this position is generally close to a confluence at the ~~victim's~~ shrinking side of the windgap (i.e., 7a). Importantly, a co-linear $\chi - z$ relation is observed for the ~~aggressor and victim~~ expanding and shrinking basins even when the stable windgap position is not at the center of the model domain (Figure 5a-d).

Figure 7a shows that, everything else being equal, the value of the area exponent m influences the position of stable windgaps. More specifically, when changing the value of the exponent m from 0.55 to 0.45, windgaps attain a stable posi-

200 tion closer to the center of the model domain. The distance between stable windgap positions with $m = 0.55$ and $m = 0.45$ typically corresponds to the distance between successive confluences.

Fixed confluence simulations based on the Parlung-Siang-Lohit setting (Figure 6), aimed to explore the effect of trunk-tributary confluences with a natural topology, show that the windgap along the beheaded Parlung Valley (with $m = 0.5$, as in the simulations of *Wang et al.* (2017) and *Yang et al.* (2018) in the same area), migrated until attaining a stable position

205 relatively close to the capture point and far from the observed location of the current windgap (i.e., points d and e in Figure 6, respectively). This stable windgap position is close to a trunk-tributary confluence on the ~~victim's~~ shrinking side (tributary t1 and point 1 in Figure 6b-c, about 150 km downstream of the observed windgap location). In contrast, in a similar experiment with a lower m value ($m = 0.45$) the windgap continued to migrate across this confluence and stopped approximately 30 km from the current natural windgap location.

210 Avulsion simulations show that avulsions influence the windgap migration velocity as well as ~~it's~~ its stable position. To compare windgap migration velocity between paired simulations with avulsions, without avulsions, and with a constant drainage area for each node, the mean windgap velocity in all models is computed up to the location where the windgap reaches a stable position in the fixed ~~confluences experiments~~ confluence simulations. Figures 5c and 7b show that in synthetic settings, avulsions increase the mean velocity of windgap migration, and that this velocity scales with the frequency of avulsions (Figure

215 7c). For the Parlung-Siang-Lohit setting, we ran a simulation without avulsions (with m=0.5) until the windgap attained the aforementioned stable position at point 1 (Figure 6b), and then forced an avulsion by shifting the drainage area of this tributary to the ~~aggressor's~~ expanding side of the windgap. This caused the windgap to migrate further east until it attained a stable position next to another large trunk-tributary confluence on the ~~victim's~~ shrinking side (point 2, just west of the confluence with tributary t2 in Figure 6b-c). Simulations with randomly occurring avulsions caused migration across these large trunk-tributary

220 confluences and ~~produce~~ produced a final stable windgap location at point 3 (Figure 6b-c), approximately 30 km from the current natural windgap location.
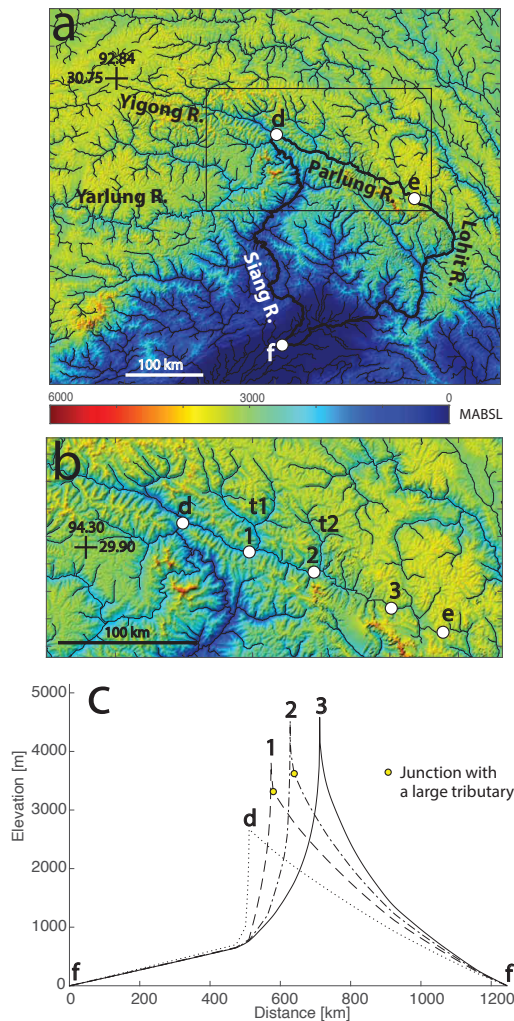
Figure 6. Simulated windgap migration along the Parlung valley. (a) Regional map, based on 15 arc-second GMTED2010 DEM (approximately 500 m resolution, (*Danielson and Gesch*, 2011)) showing the Yigong, Parlung, Lohit, Siang and Yarlung rivers (location is shown as a box in figure 2a). The approximate capture location of the Yarlung-Yigong by the Siang is marked by point d. Point e marks the current location of the windgap between the north-west flowing Parlung and south-east flowing Lohit rivers. Point f marks the base level at the confluence of the Lohit and Siang rivers. Thin dark lines mark river systems with drainage area larger than 10^8 m^2, and the bold dark lines mark the river system that is simulated in panel c. A box marks the area shown in panel b. (b) Map of the Parlung river basin. The Parlung reversed its flow direction following the capture, likely through windgap migration from the capture point (point d) to the current location of the windgap (point e). Points 1, 2 and 3 mark simulated stable windgap locations in conjunction with panel c. The labels t1, and t2, mark large tributaries of the Parlung river. (c) Profiles of simulated initial and steady-state topography. Curve d - a profile at the time of capture of the Yigong-Parlung by the Siang (the initial topography of the simulations); curve 1 - a profile of a simulated stable windgap position developed in a fixed confluence simulation. Note that this stable location is just west of a confluence with a large tributary (t1); curve 2 - a stable windgap position that developed by simulating an avulsion of tributary t1 to the expanding side of the windgap. This new stable windgap position is just west of a confluence with a large tributary t2; curve 3 - a stable windgap position that is attained through an avulsion simulation, where tributaries with drainage area larger than 10^7 m^2 are allowed to avulse. Model parameters are given in Table 1.
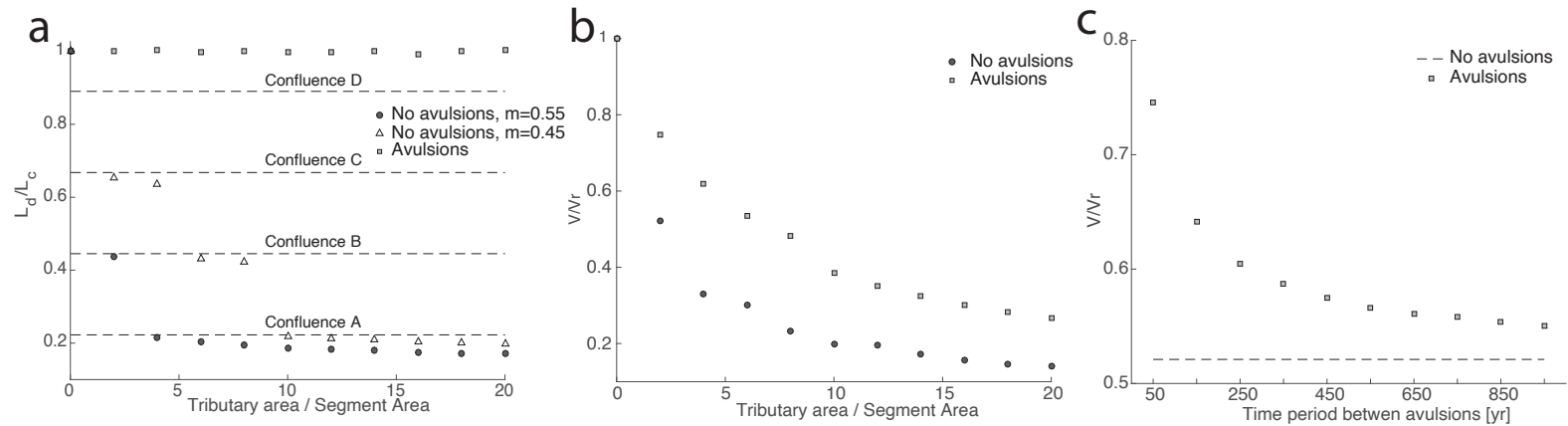
Figure 7. The influence of tributary area and avulsion frequency on windgap migration. ~~Note that every marker in panels a-c represents the results of a single simulation.~~ (a) The influence of tributary area, and the ~~value of the~~ area exponent m on the ~~relative distance between the left boundary~~ position of the ~~model domain and the~~ stable windgap ~~position. To account for tributary spacing and valley width, the drainage area of tributaries is normalized~~ relative to the ~~area~~ center of the ~~valley segment between tributaries~~ model domain (i.e., L_d/L_c, Figure 5a). ~~The windgap migration distance, L_d, is normalized by~~ When the ~~distance, L_c, between the model boundary and the center of the model domain 5a-b), such that as the windgap migrates~~ stable position is closer to ~~this~~ the center, the value L_d/L_c is closer to unity. Tributaries drainage area (A_t) is normalized by the area of the valley segment between tributaries. Note that stable windgap positions are typically next to a confluence on the ~~victim channel~~ shrinking valley side, whose location is marked by dashed horizontal lines~~, named A-D in accordance with Figure 5a. Note that when the trunk-tributary confluences are spatially fixed and the area of tributaries is relatively large, the windgap can attain a stable position relatively far from the center of the model domain, and that when avulsions are simulated, the windgap attains a stable position at the center of the model domain, similar to simulation without confluences where all nodes have the same drainage area. Also note that the distance to stable windgap locations varies with the value of the exponent m (here shown with $m=0.45$ and $m=0.55$).~~ (b) The influence of tributary area (normalized as before) on the mean velocity of windgap migration. This velocity (V) is computed based on the location and time of where/when the windgap reaches a stable position, and is normalized by the ~~duration it takes for a simulation with an equal drainage area for all nodes but the same overall model drainage area (i.e., the local drainage area at each node is the~~ mean ~~area~~ velocity (V_r) of ~~all nodes for an equivalent model~~ the reference simulation with ~~confluences) to reach~~ the same ~~location. Note that the windgap migration velocity is highest in simulations with equal~~ total drainage area~~for all nodes, and is also higher in simulations with avulsions compared to those with no avulsions~~. (c) The influence of time interval between ~~avulsion~~ avulsions on the mean velocity of windgap migration (computed ~~in~~ with the same procedure as described before), for the case where the area of tributaries is twice the segment area. The dashed line marks the velocity of an equivalent ~~simulations without avulsions~~ fixed confluence simulation. ~~The results plotted~~ Model parameters are given ~~in panels a-c rely on a model configuration with 8 trunk-tributary confluences (4 at each side of the model center), 575 model nodes, $\delta x = 100$ m, $w = 400$ m, $K = 1 \times 10^{-5}$ m^{1-2m}yr^{-1}, $n = 1$, $m = 0.45$, $D = 0.24$ m^2 yr^{-1} (for panel a also $m = 0.55$, where D is set to $D = 0.68$ m^2 yr^{-1} to maintain a constant Pécelt-based length scale with the model of $m = 0.45$ (i.e., *Perron et al., 2009*)).~~ Table 1.

5   Discussion

~~Fixed~~ fixed confluence simulations indicate that a windgap can attain a stable position that deviates from intuitive expectations. In synthetic simulations, windgaps stabilize away from the center of the model domain, despite the asymmetry in drainage area and slope associated with this position (Figure 5b). Similarly, in the natural topology simulation based on the Parlung-Siang-Lohit system, the simulated windgaps stabilize away from the present-day location of the natural windgap (~~Figures 5,~~ Figure 6). In these cases, the windgap stabilizes close to a confluence draining to the ~~victim's~~ shrinking side of the ~~windgap~~ valley (Figures 5b, 7a). From a dynamic perspective, this finding suggests that the erosion rate at this proximal confluence is approximately constant and largely independent of the windgap position. This large tributary confluence close to the ~~widngap~~windgap, counteracts the aforementioned area feedback, by balancing the erosion rates across the windgap, slowing the windgap's migration rate, and in some cases, stopping the migration process entirely and stabilizing the windgap (Figure 5c-d).

From a static perspective, stable windgap positions are possible as long as they conform to a restriction posed by a combination of channel and hillslope relief. In the context of equation 1, and assuming that D and K are spatially uniform and that the spatial transition between a hillslope and a channel is discrete (e.g., *Goren et al.*, 2014a), a windgap is stable as long as the steady-state elevation difference between the two channel heads that bound the windgap is compensated by the hillslope relief:

$$\left(\frac{U}{K}\right)^{1/n}\left|\int_0^{L_{ch1}} A_1(x')^{-m/n}\,dx' - \int_0^{L_{ch2}} A_2(x')^{-m/n}\,dx'\right| \leq \frac{U}{2D}\max(L_{h1}^2, L_{h2}^2). \tag{2}$$

The ~~LHS~~ distances between equi-elevation points along channels 1 and 2 (i.e., the location of the lower bounds of integration on the LHS) and the heads of these channels is described by L_{ch1} and L_{ch2}, respectively, and the length of the corresponding hillslope is described by L_{h1} and L_{h2}. x' represents position along channel and recognizes that drainage area (A) varies with this position. The LHS describes the absolute difference in elevation gain along the channels on both sides of the windgap (subscript 1 and 2) when the morphology of the channels is at ~~geomorphologic~~ topographic steady state and the elevation gain along each channel is integrated from the same elevation. The RHS describes the maxima of the two hillslope reliefs; between the windgap and the channel heads at each of its sides. Note that this condition holds for drainage divides in general (i.e., not only for windgaps), and that when the hilslope relief is negligible (i.e., the RHS $\simeq 0$), this condition for a stable divide simplifies to an equality in elevation gain along the two channels ~~(i.e., *Shelef and Hilley*, 2014). The distances between equi-elevation points along channels 1 and 2 (i.e., the location of the lower bounds of integration on the LHS) and the heads of these channels is described by L_{ch1} and L_{ch2}, respectively, and the length of the corresponding hillslope is described by L_{h1} and L_{h2}. x' represents position along channel and recognizes that drainage area (A) varies with this position.~~ (i.e., *Shelef and Hilley*, 2014; *Shelef*, 2018).

An example of an asymmetric and stable ~~widngap~~ windgap is depicted as case 2 in Figure 5b. The stability of this setting is verified by the co-linear $\chi - z$ relations of the channels that bound the windgap, where $\chi = \int_0^x \left(\frac{A_0}{A_1(x')}\right)^{m/n} dx'$ (e.g., *Perron and Royden*, 2013) (Figure 5d). The co-linearity of the $\chi - z$ profiles indicates that the two channels are at steady state and erode at the same rate. Here, the confluence adjacent to the windgap forms a channel head that is approximately at the same elevation as that on the aggressor's side of the windgap (channel heads were defined by the transition from concave to convex

profile). The hillslope relief is larger than the minute difference in elevation between the channel heads, and thus a stable windgap position is attained (see filled circles and bars in the $\chi - z$ plot). Generally, as long as equation 2 is satisfied, the same arrangement of confluences along a valley can produce different stable windgap positions such as those shown in Figures 5b, and 6b-c~~)~~.

260   Fixed confluence simulations with synthetic topography (Figures 5, 7a) show that the distance between stable windgap positions and the center of the model domain increases with the relative drainage area of tributaries (Figures 5b, 7a). From the static perspective of equation 2, an increase in tributaries' drainage area reduces the elevation gain along the channels and thus is more likely to facilitate situation where the hillslope relief is larger than the difference in elevation gain between the channel heads. From a dynamic perspective, and given that the simulation's initial condition is associated with a high asymmetry in

265 topographic gradient across the windgap (i.e., case 1 in Figures 5b), only confluences with relatively large tributaries are capable of balancing the shallower gradient along the ~~victim~~ shrinking side and ensure equal erosion rates across the ~~widngap~~ windgap (i.e., equation 1), stopping its migration closer to the left model boundary. A similar pattern is observed in the simulations of the Parlung-Siang-Lohit capture, where the windgap stabilizes just before it approaches confluences with large tributaries (points 1 and 2 in Figure 6b). Tributaries of a relatively small drainage area are able to stop the migration process only when the windgap

270 is closer to the center of the model domain and the overall slope asymmetry across the windgap is relatively small (Figure 7a). Similarly, a lower value of the exponent m enables windgap migration closer to the center of the model domain because it decreases the dependency of (a) fluvial erosion (i.e., equation 1), and (b) the elevation gain along steady state channels (i.e., equation 2), on the distribution of drainage area along the valley (i.e., *Shelef and Hilley*, 2014).

     The velocity of windgap migration in fixed confluence simulations changes as confluences are being traversed, and the mean

275 velocity decreases as the area of side tributaries increases (Figures 5c, 7b). The decrease in windgap velocity as it approaches a confluence reflects an increased balance in erosion rate across the windgap that stems from a relative increase in topographic gradient in the ~~victim's~~ shrinking side of the windgap, between the migrating windgap and the erosionally stable confluence. Once the windgap traverses the confluence, the tributary's discharge shifts to the ~~aggressor~~ expanding basin. This amplifies the erosion rate at the ~~aggressor's~~ expanding side of the windgap compared to the ~~victim's side , and thus~~ shrinking side and

280 increases the windgap's velocity. The duration of decreased velocity can be prolonged (or even infinite if the windgap attains a stable position) compared to the duration of increased velocity (Figure 5c). Therefore, confluences generally decrease the mean migration velocity compared to reference simulations~~(i. e., where the local drainage area is everywhere equal). .~~ This effect increases with the drainage area of side tributaries (Figure 7b), which increases the erosional stability of the confluence. Overall, our results suggest that in ~~areas~~ regions where windgaps are common, confluences with large side tributaries may be

285 critical in setting the rate of landscape adjustment to changes.

     The velocity and distance of windgap migration are influenced by the occurrence and frequency of avulsions. Stable windgap positions can be perturbed by avulsions that route discharge from the ~~victim to the aggressor~~ shrinking to the expanding basin, causing an increase in ~~the aggressor's erosion rate~~ erosion rate of the expanding basin, a decrease in ~~the victim's erosion rate~~ erosion rate of the shrinking basin, and further windgap migration (e.g., the migration of the windgap from point 1 to 2 in Figure

290 6b-c). The influence of avulsions on migration velocity is reflected in both the mean (Figures 7c) and instantaneous (Figures 5c)

migration velocity, where everything else being equal, higher avulsion frequency increases the velocity of windgap migration. ~~It is therefore possible, that~~ Note that avulsions can effectively reduce or prevent windgap slowdown before large tributaries, reducing the temporal variability in migration velocity. The expression of avulsions in the time-location space of Figure 5c, therefore depends on the frequency of avulsion and the spatial resolution of the simulation. Overall, in settings where windgap migration is common (e.g., Figure 2), ~~the rate~~ it is possible that the rate and pattern of landscape adjustment to changes in tectonic and climate depends not only on the drainage area of side tributaries, but also on the temporal frequency of avulsions in the alluvial fans at the mouth of the tributaries (e.g., Figure 4).

Avulsions in natural alluvial fans typically occur every few to thousands of years (*Field*, 2001; *Pelletier et al.*, 2005; *Fuller*, 2012). This is a relatively short time scale for large shifts in discharge across the divide given that shifts that occur through classic basin captures, as described by *Bishop* (1995); *Clark et al.* (2004); *Prince et al.* (2011); *Willett et al.* (2014), are rarely observed (e.g., *Fan et al.*, 2018). Overall, basin captures that are triggered by avulsion are likely frequent, and focusing on such settings may provide ample field examples of recent fluvial response to basin capture (e.g., Figure 4). Further, landscape evolution models tend to preserve antecedent patterns and show a relatively minor tendency for reorganization (i.e., *Kwang and Parker*, 2019). It could be that incorporating avulsion dynamics even in detachment limited settings could reveal an important component that drives models toward more realistic outcomes. Given that the frequency of avulsions depends on the micro-topography of the system, sediment characteristics, and the magnitude, burstiness, and sequencing of floods (*Field*, 2001; *Stock et al.*, 2008; *de Haas et al.*, 2016; *Leenman and Eaton*, 2020), such modeling efforts may reveal new mechanisms through which climate, lithology and tectonics influence the rate of landscape response.

~~Whereas a synthetic model without avulsions facilitates stable windgap positions that are far from the center of the model domain (Figure 7a), simulations show that avulsions trigger further windgap migration towards the center of the model domain, where the windgap attains a stable position despite continued avulsions (Figure 7a). Similarly, it is possible that avulsions helped the Parlung valley windgap to migrate across tributary confluences to its current location (i.e., point e in Figure 6b).~~ Overall, our results demonstrate that although the same arrangement of trunk-tributary confluences along a valley can generate different stable windgap positions (Figures 5, 6, 7), symmetric positions at the center of the model domain are more stable than others to perturbations caused by avulsions (~~Figures~~ Figure 7). By analogy to optimal channel networks (OCN) (e.g., *Rinaldo et al.*, 1992; *Sun et al.*, 1994a, b), stable windgap positions away from this favorable location represent local energetic optimum that, once perturbed by avulsions, develop towards a global optimum in which the windgap is close to the center of the model domain. This analogy is supported by tracking the energy dissipation over a fixed-confluence simulation that produces a stable windgap position and then perturbing it by simulating avulsions (Figure 8). From an OCN perspective, the perturbations introduced by avulsions enable the system to exit a local minima by temporally increasing the energy dissipation of the system, which is analogous to an annealing procedures (*Sun et al.*, 1994a; *Colaiori et al.*, 1997) used in OCN simulations. Thus, avulsions may act as a natural "annealing" mechanism, that shifts the landscape towards stable configurations that are energetically favorable.

Although our findings clearly demonstrate the influence of tributaries and their avulsions on wingap migration, they are based on a relatively simple set of assumptions and simulations and a limited number of field observations. For example: we

use a detachment limited model to simulate channel erosion, which was used before in similar settings (*Yang et al.*, 2020) and is consistent with the incision into bedrock in sites such as the Parlung-Siang-Lohit capture or into cohesive sediments observed in the Negev field sites (e.g., *Harel et al.*, 2019). However, given that alluvial fans are often associated with transport limited conditions (at least periodically (*Spelz et al.*, 2008)), and that valleys are often filled with unconsolidated sediments, it is likely that a model that combines detachment and transport limited processes will more accurately describe such settings. Similarly, the hillslope processes in our simulations rely on a linear diffusion approach (*Culling*, 1963) and do not account for the potential influence of subsurface flow (e.g., seepage) and landsliding on the migrating windgap (*Brocard et al.*, 2011, 2012). The simulations further neglect variabilities in the base level elevations, uplift rate, and lithology (i.e., *Harel et al.*, 2019), and they do not account for flow bifurcations that can split a tributary's discharge to multiple confluences. We also did not attempt to explore the influence of vegetation (and by extension climate), which can have competing effects of stabilizing channel banks and reducing the frequency of avulsions (*Tal and Paola*, 2010), on the one hand, and obstructing flow, and causing aggradation and avulsions (*McCarthy et al.*, 1992; *Jones and Schumm*, 1999), on the other hand. We also note that processes such as valley damming by landslides or glaciers can cause overflow across windgaps and perturb stable windgap positions. Finally, whereas our one dimensional simulations likely capture the basic dynamics of windgap migration ~~, two dimensional simulations might reveal a more detailed response~~ along valleys, they do not capture two-dimensional interactions such as drainage area exchange through divide migration along the ridgelines that bound the valley. Two-dimensional simulations might therefore reveal more detailed responses, which could depend on the 2D valley and confluence geometry.
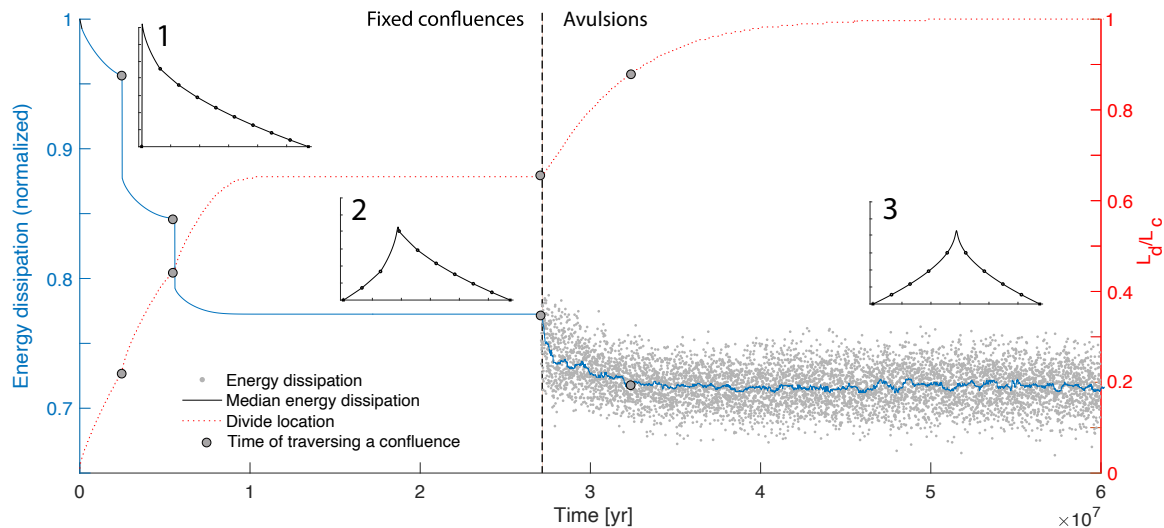
Figure 8. The influence of avulsions on energy dissipation and windgap location. Model run time is shown on the x-axis, energy dissipation (normalized by its maximal value) on the left y-axis, and ~~normalized divide~~ windgap location ~~on~~ relative to the ~~right y-axis~~ center of the model domain (i.e., L_d/L_c, ~~as in~~ Figure ~~7~~5) on the right y-axis. The plot shows the results of a fixed confluence simulation that produced a stable windgap position away from the center of the model domain at approximately ~~2.7~~1$\times10^7$ yr. An avulsion simulation introduced at ~~this point~~ approximately 2.7$\times10^7$ yr perturbed this stable topography and triggered further divide migration to the center of the model domain. ~~Avulsions~~ While avulsions can temporally increase the energy dissipation of the system, ~~for example, see the increased energy dissipation value in individual time steps (grey dots) right after the transition to an avulsion simulation. However, eventually~~ they ~~shift the system~~ lead to ~~a configuration of lower energy dissipation. Note the~~ an abrupt decrease in energy dissipation as confluences (grey circles) are being traversed. Inset images 1-3 correspond to the topographic profiles in different stages in this experiment (similar to those in Figure 5b), and show the initial topography (1), a stable asymmetric divide position attained with fixed confluence simulations (2), and a stable symmetric divide position attained with an avulsion simulation (3). ~~These simulations rely on a similar model setting and~~ Model parameters ~~as~~ are given in ~~Figure 5.~~ Table 1. The ~~relative~~ calculation of energy dissipation~~(P) was computed following (Sun et al., 1994a, b) as $P \propto \sum_i^N A_i^{1-m/n}\delta x$, where A_i is drainage area of the i'th node~~based on *Sun et al.* (1994a, b)~~, and δx is the distance between nodes. N is the number of nodes~~ described in the ~~simulation, excluding the hillslope nodes close to the windgap (defined by their convex topography)~~supplementary information. ~~Note that this approach computes the energy content of a steady state topography associated with a given distribution of drainage area.~~

6   Conclusions

In tectonically active and structurally deformed areas, where elongate valleys are common, ~~windgaps~~ low relief drainage

345   divide, windgaps, can migrate along such valleys and traverse confluences with side-tributaries that drain into the valley. These confluences are stable with respect to ~~drainage divide~~ windgap migration, namely, migration does not eradicate them, and can thus influence the migration dynamics by: (1) causing fluctuations in the velocity of windgap migration, where this velocity decreases before the windgap traverses a confluence, and increases right after it traverses the confluence; (2) facilitating

multiple configurations of stable windgap locations, aside from the perfectly symmetric configuration, where typically, the windgap stabilizes close to a confluence in the ~~victim channel~~shrinking valley. The location of these stable configurations is sensitive to the drainage area of side tributaries and the sensitivity of erosional processes to drainage area (i.e., the exponent m in Equation 1).

Avulsions of tributaries can abruptly shift discharge across the windgap, and thus change the distribution of erosion across it. Such avulsions can perturb stable windgap positions, and facilitate further windgap migration, where the velocity of windgap migration increases with the frequency of avulsions. From an energetic perspective, such avulsions may be analogous to a natural annealing mechanism, that drives the channel system towards a global energetic optimum.

Overall, our results suggest that tributaries and their avulsions may play a critical role in determining the extent of river basins in tectonically active and/or structurally deformed areas where elongate valleys are common, and thus the partitioning of discharge, erosion and sediments between these basins. Further, the rate of landscape adjustment, even in bedrock dominated mountainous regions, may be modulated by the frequency of such avulsions.

Author contributions. ES and LG conceptualized the project and designed the simulations. ES analyzed field examples, developed the code, run the simulations and analyzed them, wrote the manuscript, and prepared the figures. LG contributed to simulation interpretation and code development and provided input on the manuscript text and figures.

Competing interests. The authors declares that there is no conflict of interest

Acknowledgements. This research was supported by Grant No 2019656 from the United States-Israel Binational Science Foundation (BSF) and by Grant No. 1946253 from the United States National Science Foundation (NSF-Geomorphology and Land-use Dynamics). We thank Onn Cruvi, Elhanan Harel, Tianyue Qu, Philip Prince, and Sean Gallen for valuable discussions. TanDEM-X data were kindly provided by German Aerospace Center (DLR) (project ID: DEM_GEOL1399).

References

370 Avni, Y., Y. Bartov, Z. Garfunkel, and H. Ginat, Evolution of the Paran drainage basin and its relation to the Plio-Pleistocene history of the Arava Rift western margin, Israel., *Israel Journal of Earth Sciences*, *49*(4), https://doi.org/ 10.1560/w8wl-ju3y-km7w-8lx4, 2000.

Beeson, H. W., S. W. McCoy, and A. Keen-Zebert, Geometric disequilibrium of river basins produces long-lived transient landscapes, *Earth and Planetary Science Letters*, *475*, 34–43, https://doi.org/ 10.1016/j.epsl.2017.07.010, 2017.

Bishop, P., Drainage rearrangement by river capture, beheading and diversion, *Progress in Physical Geography*, *19*(4), 449–473,
375 https://doi.org/10.1177/030913339501900402, 1995.

Braun, J., A review of numerical modeling studies of passive margin escarpments leading to a new analytical expression for the rate of escarpment migration velocity, *Gondwana Research*, https://doi.org/10.1016/j.gr.2017.04.012, 2017.

Brocard, G., C. Teyssier, W. J. Dunlap, C. Authemayou, T. Simon-Labric, E. N. Cacao-Chiquín, A. Gutiérrez-Orrego, and S. Morán-Ical, Reorganization of a deeply incised drainage: role of deformation, sedimentation and groundwater flow, *Basin Res.*, *23*(6), 631–651,
380 https://doi.org/10.1111/j.1365-2117.2011.00510.x, 2011.

Brocard, G., et al., [rate and processes of river network rearrangement during incipient faulting: The case of the Cahabón river, Guatemala], *American Journal of Science*, *312*(5), 449–507, https://doi.org/10.2475/05.2012.01, 2012.

Clark, M. K., L. M. Schoenbohm, L. H. Royden, K. X. Whipple, B. C. Burchfiel, X. Zhang, W. Tang, E. Wang, and L. Chen, Surface uplift, tectonics, and erosion of eastern Tibet from large-scale drainage patterns, *Tectonics*, *23*(1), https://doi.org/10.1029/2002TC001402,
385 tC1006, 2004.

Colaiori, F., A. Flammini, A. Maritan, and J. R. Banavar, Analytical and numerical study of optimal channel networks, *Physical Review E*, *55*(2), 1298, https://doi.org/ 10.1103/physreve.55.1298, 1997.

Culling, W., Soil creep and the development of hillside slopes, *The Journal of Geology*, *71*(2), 127–161, https://doi.org/ 10.1086/626891, 1963.

390 Danielson, J. J., and D. B. Gesch, *Global multi-resolution terrain elevation data 2010 (GMTED2010)*, US Department of the Interior, US Geological Survey, https://doi.org/ 10.3133/ofr20111073, 2011.

Davis, W. M., A river-pirate, *Science*, *13*, 108–109, 1889.

de Haas, T., W. van den Berg, L. Braat, and M. G. Kleinhans, Autogenic avulsion, channelization and backfilling dynamics of debris-flow fans, *Sedimentology*, *63*(6), 1596–1619, https://doi.org/ 10.1111/sed.12275, 2016.

395 Fan, N., Z. Chu, L. Jiang, M. A. Hassan, M. P. Lamb, and X. Liu, Abrupt drainage basin reorganization following a pleistocene river capture, *Nature Communications*, *9*(1), 3756, https://doi.org/10.1038/s41467-018-06238-6, 2018.

Farr, T. G., et al., The shuttle radar topography mission, *Reviews of geophysics*, *45*(2), 2007.

Field, J., Channel avulsion on alluvial fans in southern Arizona, *Geomorphology*, *37*(1-2), 93–104, https://doi.org/ 10.1016/s0169-555x(00)00064-7, 2001.

400 Forte, A. M., K. X. Whipple, and E. Cowgill, Drainage network reveals patterns and history of active deformation in the eastern Greater Caucasus, *Geosphere*, *11*(5), 1343–1364, https://doi.org/10.1130/GES01121.1, 2015.

Forte, A. M., and K. X. Whipple, Criteria and tools for determining drainage divide stability, *Earth and Planetary Science Letters, 493*, 102 – 117, https://doi.org/https://doi.org/10.1016/j.epsl.2018.04.026, 2018.

Freeman, T. G., Calculating catchment area with divergent flow based on a regular grid, *Computers & Geosciences*, *17*(3), 413–422,
405 https://doi.org/ 10.1016/0098-3004(91)90048-i, 1991.

Fuller, J. E., Evaluation of avulsion potential on active alluvial fans in central and western Arizona, *Arizona Geological Survey Contributed Report -12-D*, p. 83, 2012.

Gilbert, G. K., *Report on the Geology of the Henry Mountains*, US Government Printing Office, 1877.

Ginat, H., E. Zilberman, and Y. Avni, Tectonic and paleogeographic significance of the Edom River, a Pliocene stream that crossed the Dead Sea Rift valley., *Israel Journal of Earth Sciences*, *49*(3), https://doi.org/10.1560/n2p9-ybj0-q44y-gwyn, 2000.

Goren, L., M. Fox, and S. D. Willett, Tectonics from fluvial topography using formal linear inversion: Theory and applications to the Inyo Mountains, California, *Journal of Geophysical Research: Earth Surface*, *119*(8), 1651–1681, https://doi.org/10.1002/2014JF003079, 2014a.

Goren, L., S. D. Willett, F. Herman, and J. Braun, Coupled numerical–analytical approach to landscape evolution modeling, *Earth Surface Processes and Landforms*, *39*(4), 522–545, https://doi.org/ 10.1002/esp.3514, 2014b.

Govin, G., Y. Najman, G. Dupont-Nivet, I. Millar, P. Van Der Beek, P. Huyghe, P. O'sullivan, C. Mark, and N. Vögeli, The tectonics and paleo-drainage of the easternmost Himalaya (Arunachal Pradesh, India) recorded in the Siwalik rocks of the foreland basin, *American Journal of Science*, *318*(7), 764–798, https://doi.org/tps://doi.org/10.2475/07.2018.02, 2018.

Hack, J., Studies of longitudinal profiles in Virginia and Maryland, *Survey Prof. Papers, US Government Printing Office, Washington, DC*, *690*(691), 10, https://doi.org/ 10.3133/pp294b, 1957.

Harel, E., L. Goren, E. Shelef, and H. Ginat, Drainage reversal toward cliffs induced by lateral lithologic differences, *Geology*, *47*(10), 928–932, https://doi.org/ 10.1130/g46353.1, 2019.

Haworth, R., and C. Ollier, Continental rifting and drainage reversal: the clarence river of eastern Australia, *Earth Surface Processes and Landforms*, *17*(4), 387–397, 1992.

Howard, A. D., A detachment-limited model of drainage basin evolution, *Water resources research*, *30*(7), 2261–2285, 1994.

Howard, A. D., and G. Kerby, Channel changes in badlands, *Geological Society of America Bulletin*, *94*(6), 739–752, https://doi.org/ 10.1130/0016-7606(1983)94<739:ccib>2.0.co;2, 1983.

Johnson, D. W., River capture in the Tallulah district, Georgia, *Science*, *25*(637), 428–432, 1907.

Jones, L., and S. Schumm, Causes of avulsion: an overview, *Fluvial sedimentology VI, 28*, 171–178, 1999.

Krieger, G., A. Moreira, H. Fiedler, I. Hajnsek, M. Werner, M. Younis, and M. Zink, Tandem-x: A satellite formation for high-resolution sar interferometry, *IEEE Transactions on Geoscience and Remote Sensing*, *45*(11), 3317–3341, 2007.

Kwang, J., and G. Parker, Extreme memory of initial conditions in numerical landscape evolution models, *Geophysical Research Letters*, *46*(12), 6563–6573, https://doi.org/ 10.1029/2019gl083305, 2019.

Lang, K. A., and K. W. Huntington, Antecedence of the Yarlung–Siang–Brahmaputra River, eastern Himalaya, *Earth and Planetary Science Letters*, *397*, 145–158, https://doi.org/ 10.1016/j.epsl.2014.04.026, 2014.

Leenman, A., and B. Eaton, Mechanisms for avulsion on alluvial fans: insights from high-frequency topographic data, *Earth Surface Processes and Landforms*, https://doi.org/ 10.1002/esp.5059, 2020.

Liu, L., Rejuvenation of Appalachian topography caused by subsidence-induced differential erosion, *Nat. Geosci.*, *7*(7), 518–523, 2014.

McCarthy, T., W. Ellery, and I. Stanistreet, Avulsion mechanisms on the okavango fan, botswana: the control of a fluvial system by vegetation, *Sedimentology*, *39*(5), 779–795, 1992.

Mudd, S. M., and D. J. Furbish, Lateral migration of hillcrests in response to channel incision in soil-mantled landscapes, *Journal of Geophysical Research: Earth Surface*, *110*(F4), https://doi.org/10.1029/2005JF000313, 2005.

Nugent, C., The zambezi river: tectonism, climatic change and drainage evolution, *Palaeogeogr. Palaeoclimatol. Palaeoecol.*, *78*(1), 55–69, https://doi.org/10.1016/0031-0182(90)90204-K, 1990.

445   Ollier, C. D., Tectonics and landscape evolution in southeast Australia, *Geomorphology*, *12*(1), 37–44, https://doi.org/10.1016/0169-555X(94)00075-3, 1995.

Pelletier, J. D., Persistent drainage migration in a numerical landscape evolution model, *Geophysical Research Letters*, *31*(20), https://doi.org/10.1029/2004gl020802, 2004.

Pelletier, J. D., L. Mayer, P. A. Pearthree, P. K. House, K. A. Demsey, J. E. Klawon, and K. R. Vincent, An integrated approach to flood

450   hazard assessment on alluvial fans using numerical modeling, field mapping, and remote sensing, *Geological Society of America Bulletin*, *117*(9-10), 1167–1180, https://doi.org/ 10.1130/b25544.1, 2005.

Perron, J. T., and L. Royden, An integral approach to bedrock river profile analysis, *Earth Surface Processes and Landforms*, *38*(6), 570–576, https://doi.org/10.1002/esp.3302, 2013.

Perron, J. T., W. E. Dietrich, and J. W. Kirchner, Controls on the spacing of first-order valleys, *Journal of Geophysical Research: Earth*

455   *Surface*, *113*(F4), https://doi.org/ 10.1029/2007jf000977, 2008.

Perron, J. T., J. W. Kirchner, and W. E. Dietrich, Formation of evenly spaced ridges and valleys, *Nature*, *460*(7254), 502–505, https://doi.org/10.1038/nature08174, 2009.

Prince, P. S., J. A. Spotila, and W. S. Henika, New physical evidence of the role of stream capture in active retreat of the Blue Ridge Escarpment, southern Appalachians, *Geomorphology*, *123*(3), 305 – 319, https://doi.org/ 10.1016/j.geomorph.2010.07.023, 2010.

460   Prince, P. S., J. A. Spotila, and W. S. Henika, Stream capture as driver of transient landscape evolution in a tectonically quiescent setting, *Geology*, *39*(9), 823–826, https://doi.org/10.1130/G32008.1, 2011.

Rinaldo, A., I. Rodriguez-Iturbe, R. Rigon, R. L. Bras, E. Ijjasz-Vasquez, and A. Marani, Minimum energy and fractal structures of drainage networks, *Water Resources Research*, *28*(9), 2183–2195, https://doi.org/ 10.1029/92wr00801, 1992.

Scherler, D., and W. Schwanghart, Drainage divide networks – Part 1: Identification and ordering of drainage divides in digital elevation

465   models, *Earth Surface Dynamics*, *8*(2), 245–259, https://doi.org/ 10.5194/esurf-8-245-2020, 2020a.

Schmidt, J. L., P. K. Zeitler, F. J. Pazzaglia, M. M. Tremblay, D. L. Shuster, and M. Fox, Knickpoint evolution on the Yarlung river: Evidence for late Cenozoic uplift of the southeastern Tibetan plateau margin, *Earth Planet. Sci. Lett*, *430*, 448–457, https://doi.org/10.1016/j.epsl.2015.08.041, 2015.

Seidl, M., and W. Dietrich, The problem of channel erosion into bedrock, *Functional geomorphology*, pp. 101–124, 1992.

470   Shelef, E., and G. E. Hilley, Symmetry, randomness, and process in the structure of branched channel networks, *Geophysical Research Letters*, *41*(10), 3485–3493, https://doi.org/10.1002/2014GL059816, 2014.

Shelef, E., Channel profile and plan-view controls on the aspect ratio of river basins, *Geophysical Research Letters*, *45*(21), 11–712, 2018.

Shephard, G. E., R. D. Muller, L. Liu, and M. Gurnis, Miocene drainage reversal of the Amazon River driven by plate-mantle interaction, *Nat. Geosci.*, *3*(12), 870–875, https://doi.org/10.1038/ngeo1017, 2010.

475   Spelz, R. M., J. M. Fletcher, L. A. Owen, and M. W. Caffee, Quaternary alluvial-fan development, climate and morphologic dating of fault scarps in Laguna Salada, Baja California, Mexico, *Geomorphology*, *102*(3-4), 578–594, https://doi.org/ 10.1016/j.geomorph.2008.06.001, 2008.

Stock, J. D., K. M. Schmidt, and D. M. Miller, Controls on alluvial fan long-profiles alluvial fan long-profiles, *GSA Bulletin*, *120*(5-6), 619–640, https://doi.org/ 10.1130/b26208.1, 2008.

480 Sun, T., P. Meakin, and T. Jøssang, Minimum energy dissipation model for river basin geometry, *Physical Review E*, *49*(6), 4865, https://doi.org/ 10.1103/physreve.49.4865, 1994a.

Sun, T., P. Meakin, and T. Jøssang, The topography of optimal drainage basins, *Water Resources Research*, *30*(9), 2599–2610, https://doi.org/ 10.1029/94wr01050, 1994b.

Tal, M., and C. Paola, Effects of vegetation on channel morphodynamics: results and insights from laboratory experiments, *Earth Surface*
485 *Processes and Landforms*, *35*(9), 1014–1028, 2010.

Tucker, G. E., and G. R. Hancock, Modelling landscape evolution, *Earth Surface Processes and Landforms*, *35*(1), 28–50, https://doi.org/ 10.1002/esp.1952, 2010.

Wang, Y., H. Zhang, D. Zheng, W. von Dassow, Z. Zhang, J. Yu, and J. Pang, How a stationary knickpoint is sustained: New insights into the formation of the deep Yarlung Tsangpo Gorge, *Geomorphology*, *285*, 28–43, https://doi.org/ 10.1016/j.geomorph.2017.02.005, 2017.

490 Whipple, K. X., and G. E. Tucker, Dynamics of the stream-power river incision model: Implications for height limits of mountain ranges, landscape response timescales, and research needs, *Journal of Geophysical Research: Solid Earth*, *104*(B8), 17,661–17,674, https://doi.org/ 10.1029/1999jb900120, 1999.

Whipple, K. X., A. M. Forte, R. A. DiBiase, N. M. Gasparini, and W. B. Ouimet, Timescales of landscape response to divide migration and drainage capture: Implications for the role of divide mobility in landscape evolution, *Journal of Geophysical Research: Earth Surface*,
495 *122*(1), 248–273, https://doi.org/10.1002/2016JF003973, 2017.

Willett, S. D., S. W. McCoy, J. T. Perron, L. Goren, and C.-Y. Chen, Dynamic Reorganization of River Basins, *Science*, *343*(6175), https://doi.org/10.1126/science.1248765, 2014.

Woodruff, J. C. M., Stream piracy near the balcones fault zone, central Texas, *The Journal of Geology*, *85*(4), 483–490, https://doi.org/10.1086/628322, 1977.

500 Yang, R., S. D. Willett, and L. Goren, In situ low-relief landscape formation as a result of river network disruption, *Nature*, *520*(7548), 526–529, https://doi.org/ 10.1038/nature14354, 2015.

Yang, R., F. Herman, M. G. Fellin, and C. Maden, Exhumation and topographic evolution of the Namche Barwa Syntaxis, eastern Himalaya, *Tectonophysics*, *722*, 43–52, https://doi.org/ 10.1016/j.tecto.2017.10.026, 2018.

Yang, R., et al., Early pleistocene drainage pattern changes in Eastern Tibet: Constraints from provenance analysis, thermochronometry, and
505 numerical modeling, *Earth and Planetary Science Letters*, *531*, 115,955, https://doi.org/ 10.1016/j.epsl.2019.115955, 2020.

Yanites, B. J., T. A. Ehlers, J. K. Becker, M. Schnellmann, and S. Heuberger, High magnitude and rapid incision from river capture: Rhine River, Switzerland, *J. Geophys. Res. Earth Surface*, *118*(2), 1060–1084, https://doi.org/10.1002/jgrf.20056, 2013.

Zelilidis, A., Drainage evolution in a rifted basin, Corinth graben, Greece, *Geomorphology*, *35*(1), 69–85, https://doi.org/10.1016/S0169-555X(00)00023-4, 2000.

510 Zhang, P., et al., Palaeodrainage evolution of the large rivers of East Asia, and Himalayan-Tibet tectonics, *Earth-science reviews*, *192*, 601–630, https://doi.org/ 10.1016/j.earscirev.2019.02.003, 2019.